Virtual-Axis Injection Based Online Parameter Identification of PMSM Considering Cross Coupling and Saturation Effects

Shaobo Liu, Qiwei Wang, Gaolin Wang, *Senior Member, IEEE*, Binxing Li, Dawei Ding, *Member, IEEE*, Guoqiang Zhang, *Member, IEEE*, and Dianguo Xu, *Fellow, IEEE*

***Abstract*—Existing online parameter identification methods of permanent magnet synchronous motors (PMSMs) are generally based on the voltage equations, the precision of which is affected by the cross coupling and magnetic saturation effects. In order to deal with this issue, a virtual-rotary-axis high-frequency signal injection based online parameter identification method is proposed in this article, where the cross coupling and magnetic saturation effects on the traditional *dq*-axis model are analyzed. On this basis, an optimized voltage model under the composite magnetic field rotary axis is introduced. In the proposed method, the cross-coupling angle and the *dq*-axis inductances can be identified by injecting the high-frequency signal into the constructed virtual rotary axis. In addition, the complex Simpson integral algorithm is adopted to obtain the information of the incremental and apparent inductances. Finally, the permanent magnet flux linkage can be estimated based on the composite magnetic field rotary axis voltage equations. The effectiveness and feasibility of the proposed method are verified by the experiments on a 2.2-kW PMSM drive.**

***Index Terms*—Cross coupling effect, inductance identification, magnetic saturation effect, permanent magnet flux linkage identification, virtual rotary axis injection.**

I. Introduction

PERMANENT magnet synchronous motors (PMSMs) have drawn increasing attention due to their good controllability, high efficiency, and excellent power density [1], [2], [3], [4]. In recent decades, many advanced control schemes have been proposed to meet the various application requirements. Most of these schemes strongly rely on the accurate motor parameters under different operation conditions. Generally, the PMSM parameter can be obtained by the online or offline identification. Among them, the online parameter identification estimates the real-time electrical parameters such as stator inductance and permanent magnet flux linkage, which is important for the control performance improvement as well as the health monitoring and fault diagnosing. In recent years, the online parameter identification methods of PMSM are mostly developed under the *dq*-axis, which can be further classified into two main categories, the signal injection based methods and the nonsignal-injection based methods.

In the signal injection based methods, the injection schemes can be divided into the rotor position offset injection, the high-frequency signal injection, and the *d*-axis direct current injection. On the one hand, the specific parameter could be identified independently through the signal injection [5]. In [6] and [7], rotor position offsets were injected as the disturbance signal to estimate the permanent magnet flux linkage. For reducing the influence of signal injection, *dq*-axis inductances can be estimated by the small-amplitude high-frequency voltage signal injection based equivalent impedance model [8]. On the other hand, the *d*-axis direct current was injected to construct multiple motor states, which could make *dq*-axis voltage equations reach full rank [9], [10], [11], [12], [13], [14]. Then, the parameter identification can be realized by the convergence algorithms, such as Gauss–Newton iteration [9], recursive least squares (RLS) [10], [11], or dynamic particle swarm optimization [12]. In addition, the permanent magnet flux linkage online can also be estimated by injecting the zero-voltage vector where the voltage equations of injection period and field oriented control (FOC) period were combined [15]. In sum, the signal injection based methods generally rely on the ideal *dq*-axis voltage equations, which did not give the full consideration of the nonideal factors, such as the cross coupling and magnetic saturation effects.

As for the nonsignal injection based methods, the degenerate-rank of *dq*-axis voltage equations is the main problem to be solved, which is generally dealt with by obtaining the partial motor parameters in advance. The ways of obtaining the partial parameters in advance are as follows: setting the fixed values, offline measurement, or adding temperature sensor [16], [17], [18], [19], [20], [21], [22], [23], [24], [25]. Then, the parameters can be identified by the full-rank voltage equations. To

Manuscript received 4 September 2022; revised 27 November 2022; accepted 29 December 2022. Date of publication 11 January 2023; date of current version 10 March 2023. This work was supported in part by the Research Fund for the National Natural Science Foundation of China under Grant 52125701, Grant 52207042, and Grant 52177034 and in part by the Fundamental Research Funds for the Central Universities under Grant FRFCU5710092020. Recommended for publication by Associate Editor L. V. Iyer. *(Corresponding author: Qiwei Wang.)*

The authors are with the School of Electrical Engineering and Automation, Harbin Institute of Technology, Harbin 150001, China (e-mail: liushaobohit@163.com; wqw0543@163.com; wgl818@hit.edu.cn; li_binxing@163.com; dingdawei@hit.edu.cn; zhgq@hit.edu.cn; xudiang@hit.edu.cn).

Color versions of one or more figures in this article are available at https://doi.org/10.1109/TPEL.2023.3236031.

Digital Object Identifier 10.1109/TPEL.2023.3236031

further improve the precision, some repeated iteration method is applied, such as the two time-scale affine projection algorithms [16], the two time-scale RLS [17], [18], and the Popov hyperstability theory [19]. In order to reduce the pulse width modulation cycles required for online parameter identification, the *dq*-axis inductances [23], [24] and permanent magnet flux linkage [25] can be identified according to the motor operation information in each PWM cycle. However, the nonsignal injection based methods still utilize the ideal *dq*-axis voltage equations, where the parameter identification errors caused by cross coupling and magnetic saturation effects are not taken into account.

Different from the ideal *dq*-axis voltage equations [26], [27], [28], [29], [30], there exist the cross-coupling and magnetic saturation effects in the actual PMSM drive system, which lead to the mutual inductances and the difference between the *dq*-axis incremental inductances and apparent inductances. What is more, the motor parameters change with the saturation degree of the PMSM due to the magnetic saturation effect. However, most of the online parameter identification methods based on the ideal d-q axis voltage equations ignore these nonideal factors, which lead to the parameter identification errors. These nonideal factors were considered in partial parameter identification researches. In [31] and [32], the $\alpha\beta$-axis voltage equations were used to deal with the cross-coupling effect. In [5] and [7], the influence of magnetic saturation effect on motor parameters identification was considered. However, the nonideal factors were not comprehensively analyzed. At the same time, most of them rarely consider the permanent magnet flux linkage identification under different load cases. Therefore, the research about the influence of the cross coupling and magnetic saturation effects on the PMSM online parameter identification need to be investigated further.

In order to solve the identification error caused by the cross coupling and magnetic saturation effects, this article proposes a virtual-rotary-axis high-frequency signal injection (VHFSI) based online parameter identification method. First, the influence of the cross coupling and magnetic saturation effects on the *dq*-axis model is analyzed. On this basis, an optimized voltage model under the composite magnetic field rotary axis is established considering the influence of cross coupling effect. By injecting high-frequency voltage signals into the constructed virtual rotary axis, the incremental inductances and position of the composite magnetic field rotary axis can be identified online. Meanwhile, the complex Simpson integral algorithm is adopted to obtain the information of incremental and apparent inductances. Finally, the permanent magnet flux linkage can be estimated based on the composite magnetic field rotary axis voltage equations.

The main contributions of this article are summarized as follows.

1) The proposed VHFSI based online parameter identification method is used to scan the inductances of all rotor positions in PMSM, achieving the synchronous acquisition of the incremental inductance and apparent inductance at composite magnetic field rotary axis. Compared with the traditional inductance identification method based on high-frequency signal injection [4], [8], the proposed inductance identification method fully considers the cross coupling and magnetic saturation effects. In addition, the proposed method can avoid the identification errors caused by the nonideal factors such as the inverter nonlinearity, filter delay, and parameter mismatch.
2) The cross-coupling angle can be identified online by constructing *S* curve based on the position difference between *dq*-axis and virtual rotary axis, so as to determine the position of composite magnetic field rotary axis. The proposed method can effectively solve the mutual inductances of PMSM voltage equations.
3) The influence of magnetic saturation effect on permanent magnet flux is innovatively studied. The permanent magnet flux linkage under different load cases can be estimated based on the composite magnetic field rotary axis voltage equations whose identification precision can be improved.

The rest of this article is organized as follows. In Section II, the PMSM model considering the cross coupling and magnetic saturation effects is analyzed. Then, the VHFSI based online parameter identification method is presented in Section III. Experimental results are provided in Section IV. Finally, Section V concludes this article

II. Analysis on PMSM Model Considering Cross Coupling and Magnetic Saturation Effects

A. *Analysis of Cross Coupling Effect on the* dq-*Axis Model*

Considering the cross coupling effect, the *dq*-axis stator flux linkage can be expressed as

$$\begin{bmatrix}\psi_{\mathrm{d}}\\ \psi_{\mathrm{q}}\end{bmatrix}=\begin{bmatrix}L_{\mathrm{d\_app}} & L_{\mathrm{dq\_app}}\\ L_{\mathrm{qd\_app}} & L_{\mathrm{q\_app}}\end{bmatrix}\begin{bmatrix}i_{\mathrm{d}}\\ i_{\mathrm{q}}\end{bmatrix}+\begin{bmatrix}\psi_{\mathrm{f}}\\ 0\end{bmatrix} \tag{1}$$

where ψ_{d} and ψ_{q} are the *dq*-axis stator flux linkage, $L_{\mathrm{d\_app}}$, $L_{\mathrm{q\_app}}$, $L_{\mathrm{dq\_app}}$, and $L_{\mathrm{qd\_app}}$ denote the *dq*-axis apparent self inductances and the apparent mutual inductances, ψ_{f} is the permanent magnet flux linkage, i_{d} and i_{q} are the *dq*-axis stator current components, respectively.

As can be seen from (1), the differential of *dq*-axis stator flux linkage can be calculated as

$$\frac{\mathrm{d}}{\mathrm{dt}}\begin{bmatrix}\psi_{\mathrm{d}}\\ \psi_{\mathrm{q}}\end{bmatrix}=\begin{bmatrix}L_{\mathrm{d\_inc}} & L_{\mathrm{dq\_inc}}\\ L_{\mathrm{qd\_inc}} & L_{\mathrm{q\_inc}}\end{bmatrix}\frac{\mathrm{d}}{\mathrm{dt}}\begin{bmatrix}i_{\mathrm{d}}\\ i_{\mathrm{q}}\end{bmatrix} \tag{2}$$

where $L_{\mathrm{d\_inc}}$, $L_{\mathrm{q\_inc}}$, $L_{\mathrm{dq\_inc}}$, and $L_{\mathrm{qd\_inc}}$ are the *dq*-axis incremental self inductances and mutual inductances, respectively.

As shown in (1) and (2), the cross coupling effect leads to the existence of mutual inductances between *dq*-axis. Due to the nonlinear relationship between the *dq*-axis flux linkage and current caused by the magnetic saturation effect, there is the numerical difference between the *dq*-axis incremental and apparent mutual inductances. Furthermore, there is the cross-coupling angle θ_{c} between the air-gap composite magnetic flux linkage and the permanent magnet flux linkage direction.

Fig. 1 shows the corresponding simulation results of PMSM cross coupling effect in (1) and (2), in which the *dq* and the d^n-q^n-axis denote the permanent magnet field rotary reference frames and the composite magnetic field rotary reference frames,

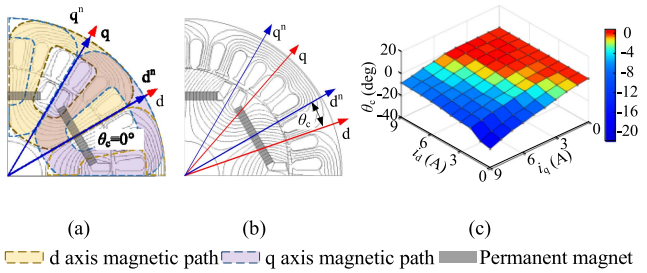

Fig. 1. Effect of cross coupling for PMSM. (a) θ_c under $i_d = 0$, $i_q = 0$. (b) θ_c under $i_d = 0$, $i_q = i_n$. (c) θ_c under different load cases.

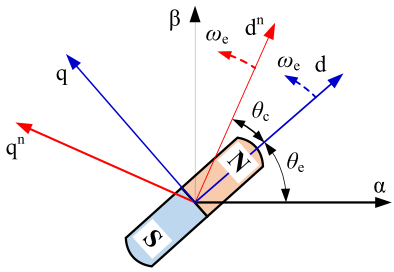

Fig. 2. PMSM reference frames considering cross coupling effect.

respectively. As shown in Fig. 1(a) and (b), the q-axis armature reaction causes cross coupling effect, which manifests θ_c between d-axis and d^n-axis by redistributing the magnetic field of yokes. As can be seen from Fig. 1(c), θ_c is 0 when the q-axis current is 0. With the increase of q-axis current or the decrease of d-axis current, the absolute value of θ_c increases.

The PMSM reference frames considering cross coupling effect are shown in Fig. 2 where the $\alpha\beta$-axis denote the stationary reference frames. The d^n-axis is in the same direction as the composite magnetic flux linkage, while the q^n-axis is perpendicular to it. There is no mutual inductance, which means there is theoretically no cross coupling between the d^n-q^n-axis.

Furthermore, considering the cross coupling effect, the stator voltage equations in the dq-axis can be expressed as

$$\begin{bmatrix} u_d \\ u_q \end{bmatrix} = R_s \begin{bmatrix} i_d \\ i_q \end{bmatrix} + \begin{bmatrix} L_{d\_inc} & L_{dq\_inc} \\ L_{qd\_inc} & L_{q\_inc} \end{bmatrix} \frac{d}{dt} \begin{bmatrix} i_d \\ i_q \end{bmatrix} + \omega_e \begin{bmatrix} -L_{qd\_app} & -L_{q\_app} \\ L_{d\_app} & L_{dq\_app} \end{bmatrix} \begin{bmatrix} i_d \\ i_q \end{bmatrix} + \omega_e \begin{bmatrix} 0 \\ \psi_f \end{bmatrix} \quad (3)$$

where u_d and u_q are the dq-axis stator voltage components, R_s denotes the stator resistance, and ω_e denotes the electrical angular velocity.

The incremental and apparent mutual inductances exist in the dq-axis voltage equations considering the cross coupling effect. Since these nonideal factors are not considered in the traditional dq-axis voltage equations, the precision of parameter identification is affected. According to (3), the inductance identification error without considering the cross coupling effect [4], [8] can be expressed by

$$\begin{cases} \varepsilon_{d\_inc} = \frac{L_{d\_inc} - \hat{L}_{d\_inc}}{L_{d\_inc}} = \frac{L_{dq\_inc}^2}{L_{d\_inc} L_{q\_inc}} \\ \varepsilon_{q\_inc} = \frac{L_{q\_inc} - \hat{L}_{q\_inc}}{L_{q\_inc}} = \frac{L_{dq\_inc}^2}{L_{d\_inc} L_{q\_inc}} \end{cases} \quad (4)$$

where ε_{d_inc} and ε_{q_inc} are the d-axis and q-axis incremental self inductances identification errors caused by the cross coupling effect, and $\hat{L}_{q\_inc}$ denote the actual d-axis and q-axis incremental self inductances identification value, respectively.

The error of cross coupling effect is also verified by the experiments.

Moreover, the precise acquisition of the maximum torque per ampere (MTPA) and maximum torque per flux (MTPF) curves and the extension of torque-speed curve are closely related to the magnetic saturation and cross coupling effects [36], [37]. The corresponding experiments are presented in Section IV.

B. Analysis of Magnetic Saturation Effect on Permanent Magnet Flux Linkage

The permanent magnet flux linkage is not only related to the rotor temperature, but also affected by the magnetic saturation effect, which is rarely studied.

The demagnetization curve of the permanent magnet shown in Fig. 1 can be expressed as

$$\phi_m = \phi_r - \Lambda_0 F_m \quad (5)$$

where ϕ_m and ϕ_r are the total magnetic flux per pole and the virtual intrinsic magnetic flux, respectively, Λ_0 denotes the internal magnetic conductivity of the permanent magnet, F_m is the magnetic motive force in the external magnetic path. For the given permanent magnet performance and size, ϕ_r and Λ_0 are both constant.

The main magnetic flux, leakage magnetic flux and total magnetic flux in the external magnetic path can be written by

$$\begin{cases} \phi_\delta = \phi_f - \phi_a = (F_m - F_a)\Lambda_\delta = (F_m - F_a)\mu_0 A_\delta \Big/ \left(l_{g\delta} + \frac{l_{f\delta}}{\mu_{rf\delta}}\right) \\ \phi_\sigma = F_m \Lambda_\sigma = F_m \mu_0 A_\sigma \Big/ \left(l_{g\sigma} + \frac{l_{f\sigma}}{\mu_{rf\sigma}}\right) \\ \phi_m = \phi_\delta + \phi_\sigma \end{cases} \quad (6)$$

where ϕ_δ, ϕ_σ, ϕ_f, and ϕ_a are the main flux, the leakage flux, the flux of the permanent magnet interlinked with the stator windings, and the armature flux generated by the armature magnetomotive force, F_a is the armature magnetomotive force, Λ_δ and Λ_σ are the permeance of main magnetic path and leakage magnetic path, A_δ and A_σ are the effective cross-sectional areas of the main magnetic path and the leakage magnetic path, $l_{g\delta}$, $l_{g\sigma}$, $l_{f\delta}$, and $l_{f\sigma}$ are equivalent air gap lengths and ferromagnetic material lengths of main magnetic path and leakage magnetic path, $\mu_{rf\delta}$ and $\mu_{rf\sigma}$ are the core relative permeability in the main magnetic path and leakage magnetic path, respectively.

According to (5) and (6), the operating points of PMSM permanent magnet under different load cases, as shown in Fig. 3, can be obtained. The point, where the ϕ_m curve intersects with the $\phi_\delta + \phi_\sigma$ curve, is the operating point of the permanent magnet.

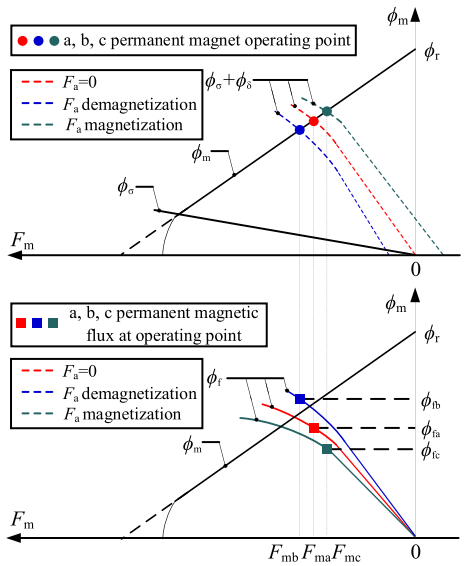

Fig. 3. Operating points of PMSM permanent magnet under different load cases.

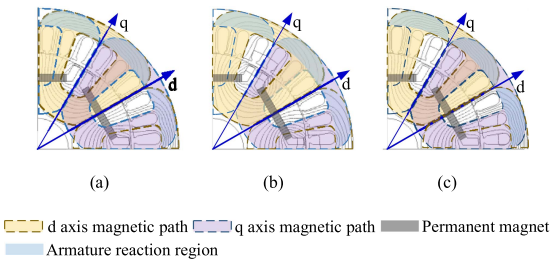

Fig. 4. Simulation results of PMSM magnetic saturation effect under different load cases. (a) $i_d = 0$, $i_q = 0$. (b) $i_d = -i_n$, $i_q = 0$. (c) $i_d = i_n$, $i_q = 0$.

Combined with the ϕ_f curve, ϕ_m can be obtained. Furthermore, the product of ϕ_m and the turns of stator winding is ψ_f.

The three operating points a, b, and c in Fig. 3 correspond to the load cases, where F_a is 0, demagnetization and magnetization, respectively. As the demagnetization effect of F_a increases, the relationship among a, b, and c is $F_{mb} < F_{ma} < F_{mc}$. In addition, F_a acting as demagnetization will lead to the increase of the ferromagnetic materials permeability. Thus, the relationship of ϕ_f at three operating points a, b, and c is $\phi_{fc} < \phi_{fa} < \phi_{fb}$. That is, ϕ_f is positively correlated with the demagnetization effect of F_a.

The simulation results of PMSM magnetic saturation effect are shown in Fig. 4, the load cases of which correspond to the three operating points a, b, and c in Fig. 3, respectively. As can be seen in Fig. 4, ψ_f increases with the increase of the weak magnetic current.

C. Optimized Voltage Equations Under Composite Magnetic Field Rotary Axis

Due to the nonideal factors, the *dq*-axis parameters number increase, and the permanent magnet flux linkage is affected by the saturation degree of magnetic path. Therefore, the composite magnetic field rotary axis voltage equations of PMSM are established in this part to consider the influence of cross coupling and magnetic saturation effects.

The *dq*-axis incremental and apparent inductance matrix shown in (1) and (2) satisfy the following conditions: 1) The diagonal elements of the inductance matrix are equal, respectively. 2) The elements in the inductance matrix are all greater than 0. Therefore, the *dq*-axis incremental and apparent inductance matrix can be seen as the positive semidefinite matrix. Hence, there must be an angle, θ_c in this case, that converts the *dq*-axis inductance matrix into the d^n-q^n-axis diagonal inductance matrix through rotation coordinate transformation $\boldsymbol{T}_{\mathbf{dq}\to\mathbf{d^nq^n}}(\theta_c)$ [34], which is

$$\boldsymbol{T}_{\mathbf{d^nq^n}\to\mathbf{dq}}(\theta_c)\begin{bmatrix} L_{d\_inc} & L_{dq\_inc} \\ L_{qd\_inc} & L_{q\_inc}\end{bmatrix}\boldsymbol{T}_{\mathbf{dq}\to\mathbf{d^nq^n}}(\theta_c) = \begin{bmatrix} L_{dn\_inc} & 0 \\ 0 & L_{qn\_inc}\end{bmatrix} \tag{7}$$

$$\boldsymbol{T}_{\mathbf{d^nq^n}\to\mathbf{dq}}(\theta_c)\begin{bmatrix} L_{d\_app} & L_{dq\_app} \\ L_{qd\_app} & L_{q\_app}\end{bmatrix}\boldsymbol{T}_{\mathbf{dq}\to\mathbf{d^nq^n}}(\theta_c) = \begin{bmatrix} L_{dn\_app} & 0 \\ 0 & L_{qn\_app}\end{bmatrix} \tag{8}$$

where L_{dn_inc} and L_{qn_inc} are the d^n-q^n-axis incremental self inductances, L_{dn_app} and L_{qn_app} denote the d^n-q^n-axis apparent self inductances, respectively. The mutual inductances in the inductance matrixes are eliminated by the proposed rotation coordinate transformation, as shown in (7) and (8).

According to (3), (7), and (8), the d^n-q^n-axis voltage equations of PMSM can be obtained as

$$\begin{bmatrix} u_{dn} \\ u_{qn}\end{bmatrix} = R_s\begin{bmatrix} i_{dn} \\ i_{qn}\end{bmatrix} + \begin{bmatrix} L_{dn\_inc} & 0 \\ 0 & L_{qn\_inc}\end{bmatrix}\frac{d}{dt}\begin{bmatrix} i_{dn} \\ i_{qn}\end{bmatrix} + \omega_e\begin{bmatrix} 0 & -L_{qn\_app} \\ L_{dn\_app} & 0\end{bmatrix}\begin{bmatrix} i_{dn} \\ i_{qn}\end{bmatrix} + \omega_e\begin{bmatrix} -\psi_f\sin\theta_c \\ \psi_f\cos\theta_c\end{bmatrix} \tag{9}$$

where i_{dn}, i_{qn}, u_{dn}, and u_{qn} are the d^n-q^n-axis stator current and voltage components, respectively.

As shown in (8), the proposed d^n-q^n-axis voltage equations contain only the self inductances. The combination of d^n-q^n-axis voltage equations and VHFSI can further realize the accurate parameters identification, which is introduced in detail in the following sections.

III. VHFSI Based Online Parameter Identification Method for PMSM Drive

A. Online Inductance Identification at Virtual Axis

In order to accurately obtain the d^n-q^n-axis PMSM parameters under different saturation conditions, this article proposes a VHFSI based online parameter identification method whose block diagram is shown in Fig. 5. The d^v-q^v virtual rotary axis is constructed, as shown in Fig. 6.

During parameter identification, the rotation frequency difference between *dq*-axis and the constructed d^v-q^v-axis, that is $\omega_e - \omega_{dv}$, is kept constant. After injecting high-frequency

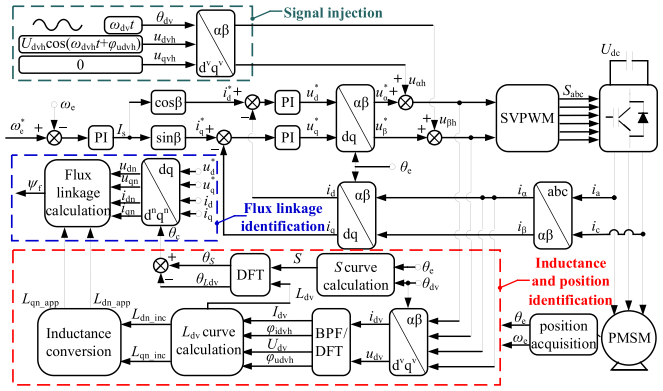

Fig. 5. Block diagram of the VHFSI based online parameter identification method.

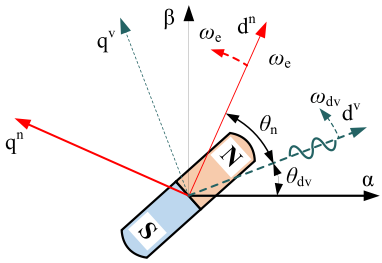

Fig. 6. Schematic diagram of virtual rotary axis.

sinusoidal voltage signal, the d^v-q^v-axis high-frequency voltage is as

$$\begin{bmatrix} u_{dvh} \\ u_{qvh} \end{bmatrix} = \begin{bmatrix} U_{dvh}\cos\left(\omega_{dvh}t+\varphi_{udvh}\right) \\ 0 \end{bmatrix} \tag{10}$$

where U_{dvh}, ω_{dvh}, and φ_{udvh} are the amplitude, frequency, and phase of the high-frequency sinusoidal voltage signal injected into the d^v-axis, respectively.

Through the rotation coordinate transformation, the d^v-q^v-axis voltage equations can be obtained from (9), which can be expressed as

$$\begin{bmatrix} u_{dv} \\ u_{qv} \end{bmatrix} = R_s \begin{bmatrix} i_{dv} \\ i_{qv} \end{bmatrix} + \mathbf{L}_{dqv\_inc}\frac{d}{dt}\begin{bmatrix} i_{dv} \\ i_{qv} \end{bmatrix} + \omega_e \mathbf{L}_{dqv\_app}\begin{bmatrix} i_{dv} \\ i_{qv} \end{bmatrix} + \omega_e\psi_f\begin{bmatrix} -\sin\theta_c\cos\theta_n - \cos\theta_c\sin\theta_n \\ \cos\theta_c\cos\theta_n - \sin\theta_c\sin\theta_n \end{bmatrix} \tag{11}$$

$$\mathbf{L}_{dqv\_inc} = \begin{bmatrix} L_{dn\_inc}\cos^2\theta_n + L_{qn\_inc}\sin^2\theta_n & \left(L_{dn\_inc}-L_{qn\_inc}\right)\sin\theta_n\cos\theta_n \\ \left(L_{dn\_inc}-L_{qn\_inc}\right)\sin\theta_n\cos\theta_n & L_{dn\_inc}\sin^2\theta_n + L_{qn\_inc}\cos^2\theta_n \end{bmatrix} \tag{12}$$

$$\mathbf{L}_{dqv\_app} = \begin{bmatrix} \left(L_{qn\_app}-L_{dn\_app}\right)\sin\theta_n\cos\theta_n \\ -L_{dn\_app}\sin^2\theta_n - L_{qn\_app}\cos^2\theta_n \\ L_{dn\_app}\cos^2\theta_n + L_{qn\_app}\sin^2\theta_n \\ \left(L_{dn\_app}-L_{qn\_app}\right)\sin\theta_n\cos\theta_n \end{bmatrix} \tag{13}$$

where θ_n is the position difference between d^n-q^n and d^v-q^v axes, $\boldsymbol{L}_{dqv\_inc}$ and $\boldsymbol{L}_{dqv\_app}$ are the d^v-q^v-axis incremental and

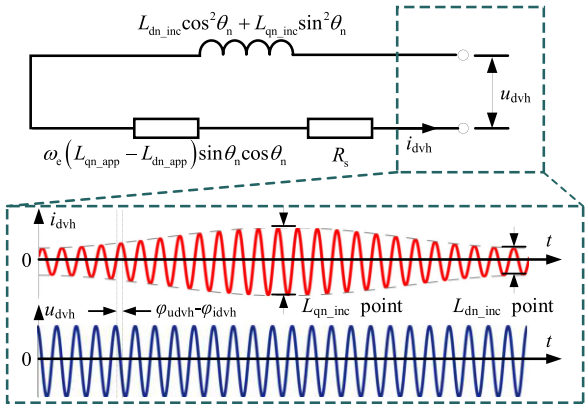

Fig. 7. d^v-axis high-frequency equivalent circuit.

apparent inductance matrices, u_{dv}, u_{qv}, i_{dv}, and i_{qv} are the d^v-q^v-axis stator voltage and current components, respectively.

Since the high-frequency signal only exist in the d^v-axis, the expression of the high-frequency current response signal can be obtained from (10) to (13) as

$$i_{dvh} = \frac{U_{dvh}}{Z_{dvh}}\cos\left(\omega_{dvh}t+\varphi_{idvh}\right) \tag{14}$$

$$Z_{dvh} = \sqrt{\begin{matrix}\left(R_s+\omega_e\left(L_{qn\_app}-L_{dn\_app}\right)\sin\theta_n\cos\theta_n\right)^2 \\ +\omega_{dvh}^2\left(L_{dn\_inc}\cos^2\theta_n + L_{qn\_inc}\sin^2\theta_n\right)^2\end{matrix}} \tag{15}$$

$$\varphi_{udvh}-\varphi_{idvh} = \arctan\frac{\omega_{dvh}\left(L_{dn\_inc}\cos^2\theta_n + L_{qn\_inc}\sin^2\theta_n\right)}{R_s+\omega_e\left(L_{qn\_app}-L_{dn\_app}\right)\sin\theta_n\cos\theta_n} \tag{16}$$

where φ_{idvh} is the phase of d^v-axis high-frequency current response signal, Z_{dvh} denotes the impedance at the d^v-axis injection frequency ω_{dvh}, which includes the equivalent resistance and equivalent inductive impedance shown in (15), $\varphi_{udvh}-\varphi_{idvh}$ is the d^v-axis impedance angle, which is the phase difference between the d^v-axis high-frequency voltage and current.

According to (14)–(16), the d^v-axis high-frequency circuit can be equivalent to the resistance and inductance in series, as shown in Fig. 7. There is the phase difference between high-frequency voltage and current. In addition, since the inductance changes with the rotor position, the amplitude of the high-frequency current response changes accordingly. Furthermore, the amplitude and phase of d^v-axis high-frequency sinusoidal voltage and current signal can be extracted by the discrete Fourier transform (DFT), where the d^v-axis inductance identification value can be obtained as

$$\begin{aligned} L_{dv} &= \frac{U_{dvh}}{I_{dvh}\omega_{dvh}}\sin\left(\varphi_{udvh}-\varphi_{idvh}\right) \\ &= \frac{L_{dn\_inc}-L_{qn\_inc}}{2}\cos 2\theta_n + \frac{L_{dn\_inc}+L_{qn\_inc}}{2}. \end{aligned} \tag{17}$$

It worth mentioning that the VHFSI based online parameter identification method is not affected by the inverter nonlinearity.

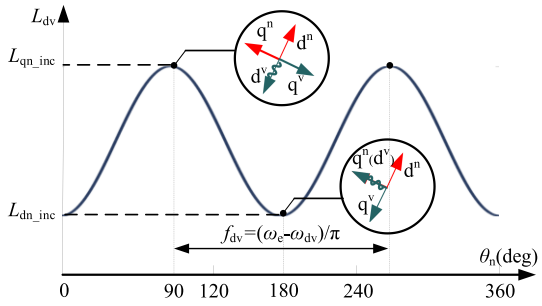

Fig. 8. Curve of L_{dv} as θ_n varies schematic diagram.

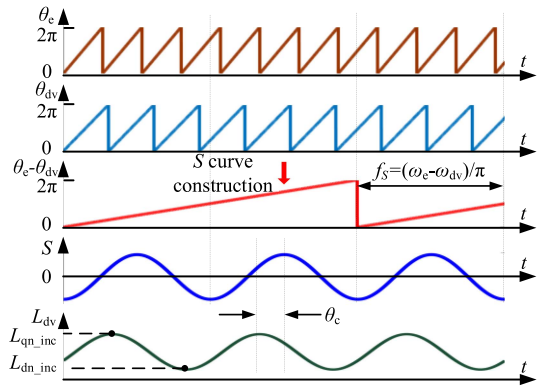

Fig. 9. Schematic diagram of online cross-coupling angle identification method.

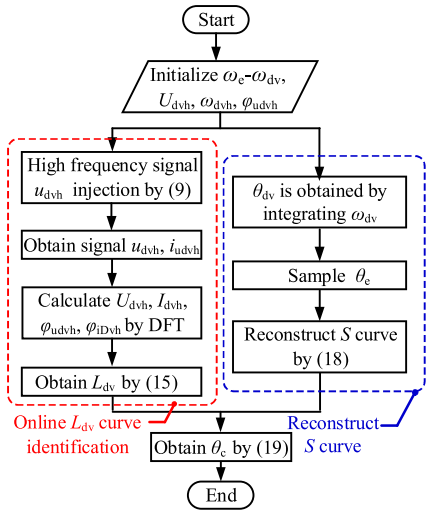

Fig. 10. Flowchart of online cross-coupling angle identification method.

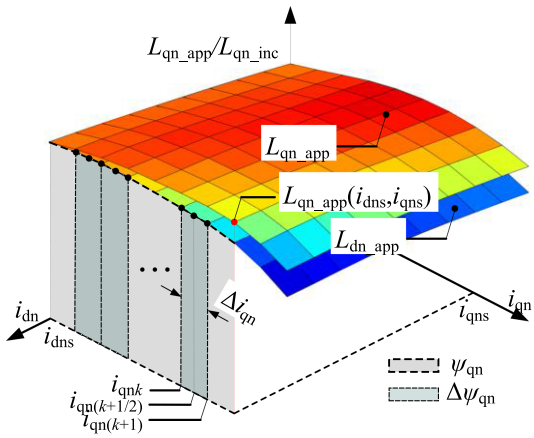

Fig. 11. Schematic diagram of apparent inductance and incremental inductance conversion based on complex Simpson integral method solving stator flux linkage.

For high-frequency signal injection, the inverter nonlinearity is generally equivalent to the resistance. As shown in (17), the resistance and inductance can be decoupled by considering the phase of high-frequency voltage and current, thus improving the accuracy of inductance identification.

In Fig. 6, there is the fixed difference between the rotational frequencies of d^n-q^n-axis and d^v-q^v-axis, which is $\theta_n = (\omega_e - \omega_{dv})t + \theta_c$. Thus, the d^v-axis inductance at any rotor position can be obtained from (17). The curve of L_{dv} as θ_n varies schematic diagram can be obtained shown in Fig. 8. The lowest point and the highest point of L_{dv} curve correspond to L_{dn_inc} and L_{qn_inc}, respectively, and the frequency of L_{dv} curve is $(\omega_e - \omega_{dv})/\pi$.

The operation frequency of DFT used for L_{dv} identification is the same as the injected high-frequency voltage signal. The number of L_{dv} points calculated by DFT in each cycle L_{dv} curve is

$$N_{dv} = \frac{\omega_{dvh}/2\pi}{(\omega_e - \omega_{dv})/\pi} = \frac{\omega_{dvh}}{2(\omega_e - \omega_{dv})} \tag{18}$$

where N_{dv} is the number of L_{dv} points calculated by DFT in each cycle L_{dv} curve.

According to (18), when ω_{dvh} remains unchanged, N_{dv} decreases and L_{dv} curve frequency increases with the increase of $\omega_e - \omega_{dv}$, which will affect the identification speed and precision of L_{dn_inc} and L_{qn_inc}. Therefore, the selection of ω_{dv} should guarantee both the convergence rate and the accuracy. In this article, $\omega_{dv} = (\omega_e + 2\pi)$rad/s is selected, where the difference between the rotational frequencies of d^n-q^n-axis and d^v-q^v-axis can be selected as 1–5 Hz.

It should be noted that, since BPF and DFT are applied in the proposed method, as shown in Fig. 5, the delay of which should also be considered to improve the identification accuracy. For the delay of BPF, it can be reduced by properly setting the bandwidth of BPF. For the delay of DFT, its delay is fixed and small which can be directly compensated online.

B. Online Identification of Cross-Coupling Angle

For achieving flux linkage identification under d^n-q^n-axis, it is necessary to realize the identification of the d^n-q^n-axis position in addition to the identification of d^n-q^n-axis inductances. In this part, a cross-coupling angle identification method based on sinusoidal signal reconstruction is proposed.

The above L_{dv} curve contains not only the d^n-q^n-axis inductances information, but also the d^n-q^n-axis position information. The d^n-axis and q^n-axis positions correspond to the phases of the

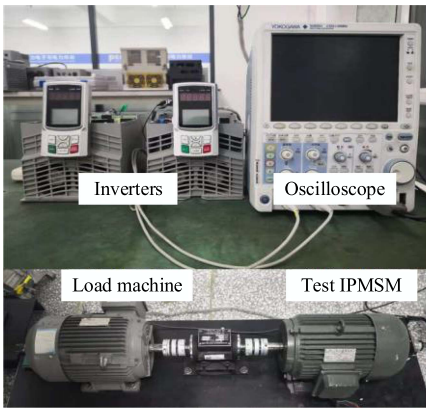

Fig. 12. 2.2-kW IPMSM drive experimental platform.

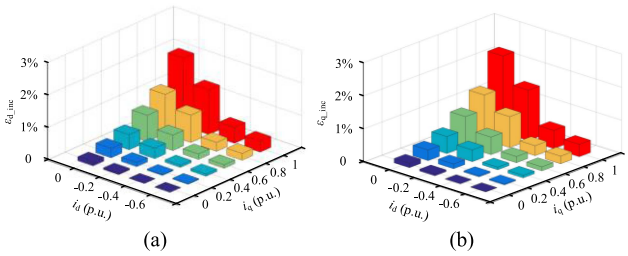

Fig. 13. Experimental results of the *dq*-axis incremental self inductance identification errors caused by cross coupling effect. (a) *d*-axis. (b) *q*-axis.

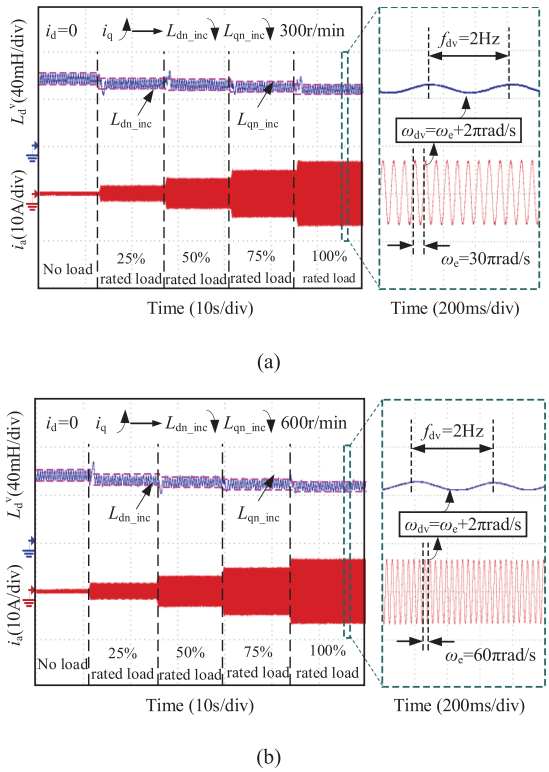

Fig. 14. Experimental results of the proposed VHFSI based online inductance identification method under $i_{\mathrm{d}} = 0$ A. (a) 300 r/min. (b) 600 r/min.

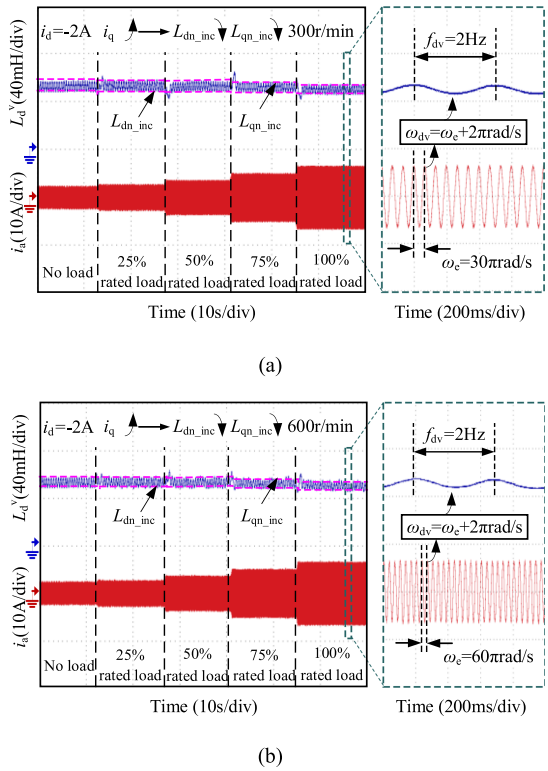

Fig. 15. Experimental results of the proposed VHFSI based online inductance identification method under $i_{\mathrm{d}} = -2$ A. (a) 300 r/min. (b) 600 r/min.

TABLE I
IPMSM PARAMETERS

Parameter	Value	Parameter	Value
Rated Power	2.2kW	Resistance	2.82Ω
Rated Speed	1000r/min	*d*-axis inductance	35.0mH
Rated Frequency	50Hz	*q*-axis inductance	64.0mH
Rated Current	5.6A	Flux linkage	0.800Wb
Rated Torque	21N·m	Number of Pole Pairs	3

minimum and maximum values of the L_{dv} curve respectively, which need to be determined by the *dq*-axis positions.

In PMSM drive system, θ_{e} can be obtained by position sensor or position observation algorithm, where the d^n-q^n-axis position can be determined by obtaining θ_{c}. As shown in Fig. 9, the trigonometric waveform can be constructed from the position difference between d^v-q^v-axis and *dq*-axis, which can be expressed as

$$S = -\cos 2\left(\theta_{\mathrm{e}} - \theta_{\mathrm{dv}}\right) = -\cos 2\left(\omega_{\mathrm{e}} - \omega_{\mathrm{dv}}\right) t \tag{19}$$

where θ_{dv} is the d^v−axis position.

Then, the phase relationship between curve $L_{\mathrm{d}}{}^{\mathrm{v}}$ and *S*, as shown in Fig. 9, can be obtained from (17) and (19). The phases of L_{dv} curve and *S* curve can be obtained by DFT as $\theta_{L\mathrm{dv}}$ and θ_S, respectively. The phase difference between L_{dv} curve and reconstructed waveform is the cross-coupling angle θ_{c}, which can be expressed as

$$\theta_{\mathrm{c}} = \theta_S - \theta_{L\mathrm{dv}}. \tag{20}$$

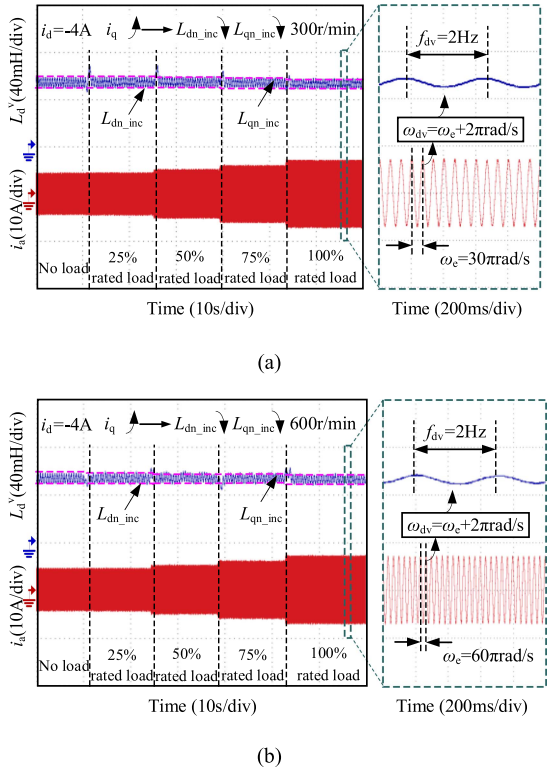

Fig. 16. Experimental results of the proposed VHFSI based online inductance identification method under $i_d = -4$ A. (a) 300 r/min. (b) 600 r/min.

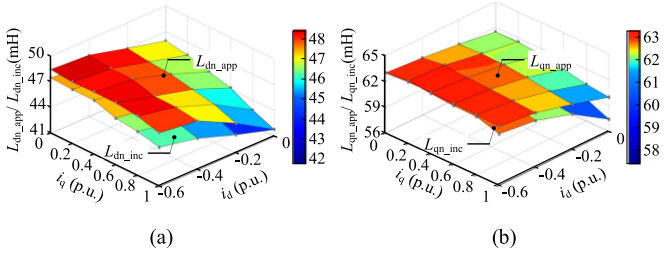

Fig. 17. d^n-q^n-axis online identification results of incremental inductances and apparent inductances conversion results of PMSM. (a) d^n-axis. (b) q^n-axis.

Fig. 10 shows the flowchart of online cross-coupling angle identification method. By constructing the virtual rotary d^v-q^v-axis, the inductances of all rotor positions are scanned and identified through VHFSI, so as to obtain the L_{dv} curve online. At the same time, S curve is reconstructed from the known positions of dq and d^v-q^v-axis. The phase difference between the L_{dv} curve and the reconstructed S curve is the cross-coupling angle. Thus, the exact position of the d^n-q^n-axis can be obtained.

C. Inductance Transformation and Permanent Magnet Flux Linkage Identification

In steady state, L_{dn_app} and L_{qn_app} are used for the flux linkage identification under d^n-q^n-axis shown in (9). Therefore, the identified L_{dn_inc} and L_{qn_inc} need to be transformed into L_{dn_app} and L_{qn_app}. In this part, an inductance transformation

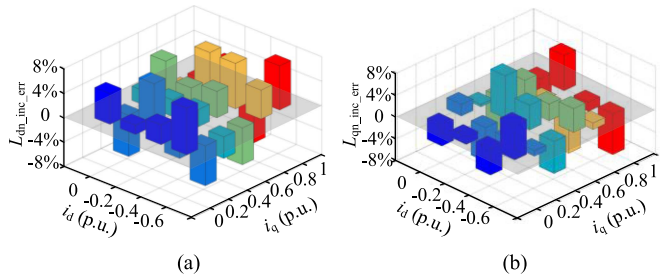

Fig. 18. d^n-q^n-axis incremental inductances online identification results error of PMSM. (a) d^n-axis. (b) q^n-axis.

method based on complex Simpson integral method solving stator flux linkage is proposed.

The relationship of d^n-q^n-axis incremental inductances and apparent inductances can be expressed as

$$\begin{cases} L_{\mathrm{x\_inc}} = d\psi_{\mathrm{x}}/di_{\mathrm{x}} \\ L_{\mathrm{x\_app}} = \psi_{\mathrm{x}}/i_{\mathrm{x}} \end{cases} \mathrm{x} = \mathrm{d^n}, \mathrm{q^n} \tag{21}$$

where ψ_{dn} and ψ_{qn} are the d^n-q^n-axis flux linkage by the d^n-axis and q^n-axis current excitation, respectively.

Then, (21) can be transformed as [35]

$$L_{\mathrm{x\_app}} = \frac{\int_0^{i_{\mathrm{xs}}} L_{\mathrm{x\_inc}} di_{\mathrm{x}}}{i_{\mathrm{x}}} \mathrm{x} = \mathrm{d^n}, \mathrm{q^n} \tag{22}$$

where i_{xs} is the current at the point of working condition to be calculated.

Here, the complex Simpson integral method is used to numerically quadrature ψ_{x} of the required operating condition, by which the $\mathrm{d^n}$-$\mathrm{q^n}$ apparent inductances are obtained online.

Fig. 11 shows the Simpson integral method for the inductance conversion. In order to obtain the q^n-axis apparent inductance $L_{\mathrm{qn\_app}}(i_{\mathrm{dns}}, i_{\mathrm{qns}})$, the integral interval $(0, i_{\mathrm{qns}})$ is divided into n equal parts. The length of each subinterval is h_{qn}. In the subinterval $(i_{\mathrm{qn}k}, i_{\mathrm{qn}(k+1)})$, the three $L_{\mathrm{qn\_inc}}$ online identification points corresponding to $i_{\mathrm{qn}k}$, $i_{\mathrm{qn}(k+1)}$, and their midpoint $i_{\mathrm{qn}(k+1/2)}$ are substituted into Simpson formula to obtain the integral value. Then, by summing the integral values of all subintervals as the approximate values of ψ_{qn} under i_{dns} and i_{qns} condition, $L_{\mathrm{qn\_app}}(i_{\mathrm{dns}}, i_{\mathrm{qns}})$ can be obtained. The expression of $L_{\mathrm{qn\_app}}(i_{\mathrm{dns}}, i_{\mathrm{qns}})$ based on the complex Simpson integral method is

$$\begin{aligned} L_{\mathrm{qn\_app}}(i_{\mathrm{dns}}, i_{\mathrm{qns}}) = {} & \frac{h_{\mathrm{qn}}}{6} L_{\mathrm{qn\_inc}}(i_{\mathrm{dns}}, i_{\mathrm{qns}}) \\ & + \frac{h_{\mathrm{qn}}}{3} \sum_{k=1}^{n-1} L_{\mathrm{qn\_inc}}(i_{\mathrm{dns}}, i_{\mathrm{qn}k}) \\ & + \frac{2h_{\mathrm{qn}}}{3} \sum_{k=0}^{n-1} L_{\mathrm{qn\_inc}}\left(i_{\mathrm{dns}}, i_{\mathrm{qn}(k+1/2)}\right). \end{aligned} \tag{23}$$

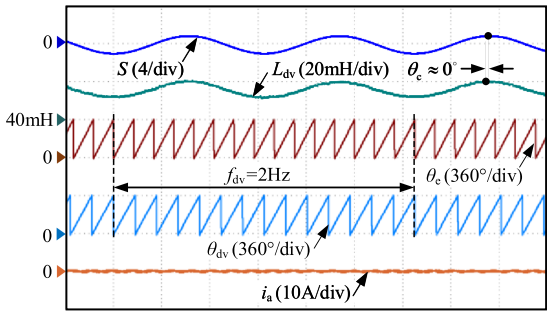

(a)

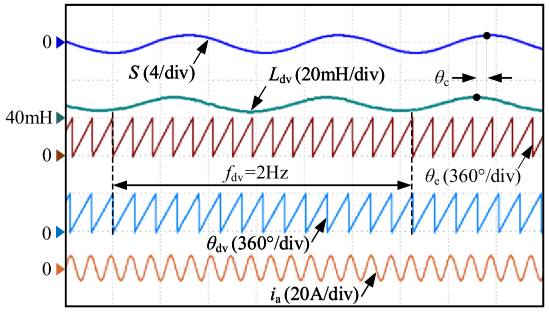

(b)

Fig. 19. Experimental results of online cross-coupling angle identification when speed is 300 r/min and $i_d = 0$ A. (a) No load. (b) 100% rated load.

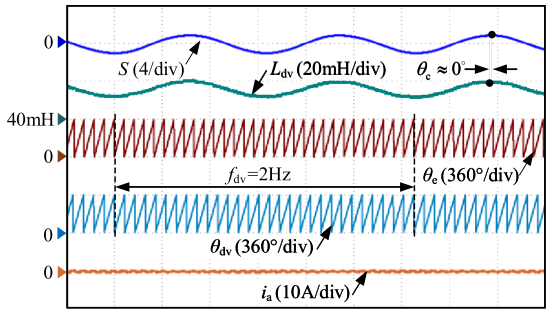

(a)

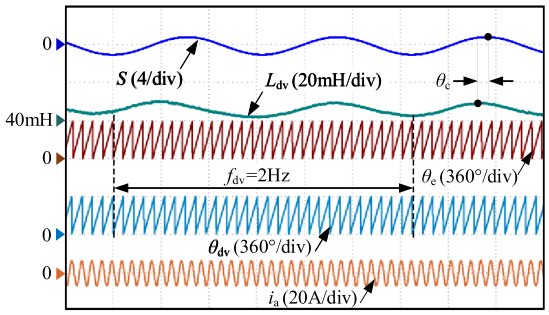

(b)

Fig. 20. Experimental results of online cross-coupling angle identification when speed is 600 r/min and $i_d = 0$ A. (a) No load. (b) 100% rated load.

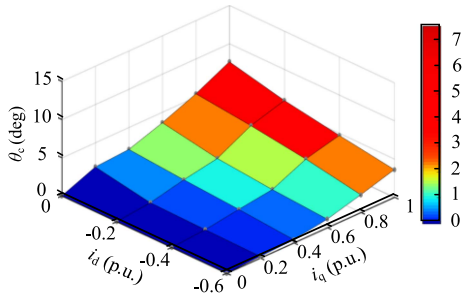

Fig. 21. Online identification results of PMSM cross-coupling angle.

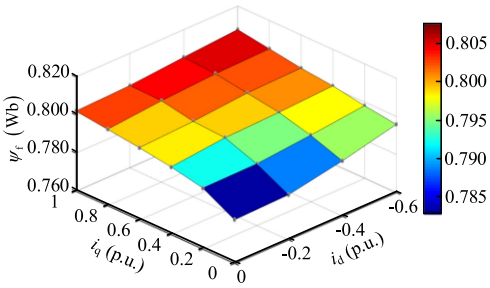

Fig. 22. Online identification experimental results of PMSM permanent magnet flux linkage in d^n-q^n-axis.

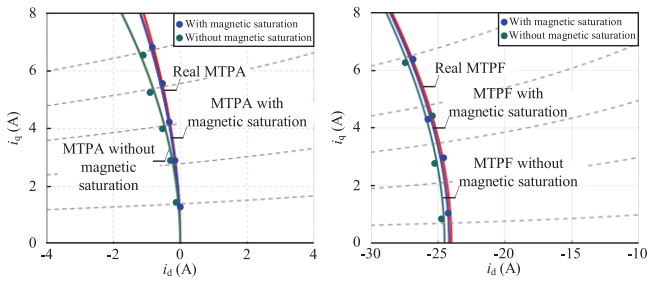

Fig. 23. Experimental results of MTPA and MTPF control with and without considering cross coupling and magnetic saturation effects. (a) Experimental results of MTPA. (b) Experimental results of MTPF.

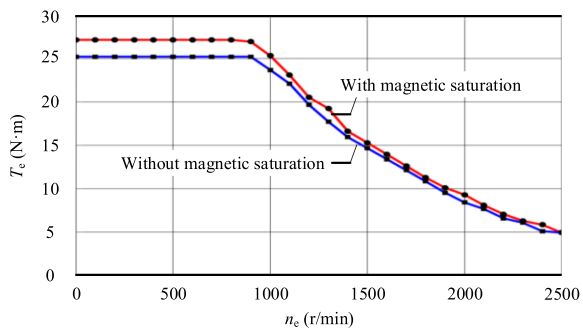

Fig. 24. Torque-speed curves with and without considering cross coupling and magnetic saturation effects.

Similarly, the expression of $L_{\mathrm{dn\_app}}(i_{\mathrm{dns}},i_{\mathrm{qns}})$ based on complex Simpson integral method i_{dns} and i_{qns} condition is

$$\begin{aligned} L_{\mathrm{dn\_app}}\left(i_{\mathrm{dns}},i_{\mathrm{qns}}\right) = {} & \frac{h_{\mathrm{dn}}}{6}L_{\mathrm{dn\_inc}}\left(i_{\mathrm{dns}},i_{\mathrm{qns}}\right) \\ & + \frac{h_{\mathrm{dn}}}{3}\sum_{k=1}^{n-1}L_{\mathrm{dn\_inc}}\left(i_{\mathrm{dns}},i_{\mathrm{qn}k}\right) \\ & + \frac{2h_{\mathrm{dn}}}{3}\sum_{k=0}^{n-1}L_{\mathrm{dn\_inc}}\left(i_{\mathrm{dns}},i_{\mathrm{qn}(k+1/2)}\right) \end{aligned} \tag{24}$$

where h_{dn} is the subinterval length after dividing the integral interval $(0, i_{\mathrm{dns}})$ into n equal parts.

On the basis that the $d^n q^n$-axis position and apparent inductances have been obtained by the abovementioned method, the d^n-q^n-axis calculation formula of permanent magnet flux linkage in steady state can be obtained from (9), which can be expressed as

$$\psi_{\mathrm{f}} = \frac{\sqrt{\left(u_{\mathrm{dn}}-R_{\mathrm{s}}i_{\mathrm{dn}}+\omega_{\mathrm{e}}L_{\mathrm{qn\_app}}i_{\mathrm{qn}}\right)^2+\left(u_{\mathrm{qn}}-R_{\mathrm{s}}i_{\mathrm{qn}}-L_{\mathrm{dn\_app}}i_{\mathrm{dn}}\right)^2}}{\omega_{\mathrm{e}}}. \tag{25}$$

According to (9) and (25), the mutual inductances term in permanent magnet flux linkage identification can be dealt with by using d^n-q^n-axis voltage equations.

IV. Experimental Results

The proposed VHFSI based online parameter identification method is verified on the experimental platforms, as shown in Fig. 12. The parameters of the test PMSM are listed in Table I. The PWM carrier frequency is set as 6 kHz. The corresponding algorithm is realized by STM32F103.

Fig. 13 shows the experimental results of the dq-axis incremental self inductance identification errors caused by cross coupling effect, where the inductances identification method is consistent with [4] and [8]. According to the experimental results, the maximum inductance identification error caused by the cross coupling effect can reach 2%, while the maximum inductance identification error in [4] and [8] is 6%. Under the heavy load condition, the accuracy of inductance identification can be significantly improved if the cross coupling effect is fully considered.

Figs. 14–16 show the experimental results of the proposed VHFSI based online inductance identification method under different working conditions, where the load changes from no-load to 100% rated load with 20% rated load interval. As shown in the results, the rotation frequency of the constructed virtual axis is set to be 1 Hz different from the operating frequency of the motor. In the experimental results, the inductance curves frequency obtained under different working conditions is 2 Hz, where the identification speed and accuracy of the inductance curves are taken into account. At the same time, the high-frequency voltage injected in the d^v-axis is selected as 500 Hz.

Taking Fig. 14 as an example, the maximum value and minimum value of the obtained L_{dv} curve are the $L_{\mathrm{qn\_inc}}$ and $L_{\mathrm{dn\_inc}}$ respectively. Under the condition of $i_{\mathrm{d}} = 0$ A, with the increase of load, both $L_{\mathrm{qn\_inc}}$ and $L_{\mathrm{dn\_inc}}$ decrease due to magnetic circuit saturation. When the load increases from no load to 100% rated load, $L_{\mathrm{qn\_inc}}$ decreases from 60.3 to 50.4 mH and $L_{\mathrm{dn\_inc}}$ decreases from 52.4 to 45.3 mH. Moreover, the inductance identification results are not affected by the speed, in which the proposed method shows strong robustness.

According to Fig. 17, the $L_{\mathrm{q}^{\mathrm{n}}\_\mathrm{inc}}$ and $L_{\mathrm{d}^{\mathrm{n}}\_\mathrm{inc}}$ surfaces under different load cases can be directly obtained from the experimental data shown in Figs. 14–16. The $L_{\mathrm{q}^{\mathrm{n}}\_\mathrm{app}}$ and $L_{\mathrm{d}^{\mathrm{n}}\_\mathrm{app}}$ surfaces can further be obtained by the proposed complex Simpson integral based inductance transformation method and the $L_{\mathrm{q}^{\mathrm{n}}\_\mathrm{inc}}$ and $L_{\mathrm{d}^{\mathrm{n}}\_\mathrm{inc}}$ surfaces. As can be seen in Fig. 17, there are differences between d^n-q^n-axis incremental inductances and apparent inductances under different dq-axis current combination. In addition, the inductances used in permanent magnet flux identification in (25) are the apparent inductances. The conversion results of apparent inductance for permanent magnet flux identification fully consider the cross coupling and magnetic saturation effects in the actual motor system.

By comparing the d^n-q^n-axis online inductances identification results with the finite element simulation results, the d^n-q^n-axis incremental inductances online identification results error of PMSM, as shown in Fig. 18, can be obtained. According to Fig. 18, the d^n-q^n-axis incremental inductances identification error is within 8%. The effectiveness and feasibility of the proposed online identification method can be further verified.

Figs. 19 and 20 show the experimental results of online cross-coupling angle identification under different speeds. Taking Fig. 20 as an example, the average phase difference between S curve and L_{dv} is 0.9° when $i_{\mathrm{d}} = 0$ A and no load. However, it is 7.6° when $i_{\mathrm{d}} = 0$ A and 100% rated load. The cross-coupling angle can be effectively identified online by the proposed method, the results of which are shown in Fig. 21. As shown in Fig. 21, the cross-coupling angle increases with the increase of q-axis current and the decrease of d-axis demagnetization current. Accordingly, the position of d^n-q^n-axis is determined.

The online identification experimental results of PMSM permanent magnet flux in d^n-q^n-axis are shown in Fig. 22. The identification results of permanent magnet flux linkage obtained by the proposed method are approximately similar to the nameplate value. With the increase of the flux-weakening current, the online identification results of permanent magnet flux linkage increase from 0.782 Wb to 0.807 Wb, which is consistent with the theoretical analysis result in Section II-B.

To prove the usefulness of the proposed method further in practice, the identified parameters are used in the PMSM control strategy, where the corresponding experimental results are shown in the Figs. 23 to 24. Fig. 23 shows the experiment results of MTPA and MTPF control with and without considering cross coupling and magnetic saturation effects. According to the experimental results shown in Fig. 23(a), the difference of MTPA curves with and without considering cross coupling and magnetic saturation effects becomes larger with the increase of load torque. According to the experimental results shown in

Fig. 23(b) shows the MTPF control experiment results with and without the magnetic saturation effect, the MTPF curve cross coupling and magnetic saturation effects is closer to the real MTPF curve.

Fig. 24 shows the torque-speed curves of PMSM with and without magnetic saturation effect. It can be seen from the comparison that the control accuracy of PMSM can be improved by considering magnetic saturation and cross coupling effects. What is more, the torque-speed envelope is also expected. The effectiveness and feasibility of the proposed method can be further verified.

V. Conclusion

In this article, a novel VHFSI based online parameter identification method has been proposed. By injecting high-frequency voltage signal into the constructed virtual axis, the d^n-q^n-axis incremental inductances surface and position of PMSM have been accurately identified online. Furthermore, the apparent inductances surface has been obtained by the complex Simpson integral method. Compared with the traditional method, the cross coupling and magnetic saturation effects have been fully considered in the proposed method. Meanwhile, the permanent magnet flux linkage has been accurately identified, where the influence of the magnetic saturation conditions has been fully considered. The proposed parameter identification method can accurately identify the parameters of PMSM under different saturation, which is suitable for the motor drive system with and without position sensor.

References

[1] G. Wang, R. Yang, and D. Xu, "DSP-based control of sensorless IPMSM drives for wide-speed range operation," *IEEE Trans. Ind. Electron.*, vol. 60, no. 2, pp. 720–727, Feb. 2013.

[2] L. Sun, X. Li, and L. Chen, "Motor speed control with convex optimization-based position estimation in the current loop," *IEEE Trans. Power Electron.*, vol. 36, no. 9, pp. 10906–10919, Sep. 2021.

[3] L. Qu, W. Qiao, and L. Qu, "Active-disturbance-rejection-based sliding-mode current control for permanent-magnet synchronous motors," *IEEE Trans. Power Electron.*, vol. 36, no. 1, pp. 751–760, Jan. 2021.

[4] G. Wang et al., "Self-commissioning of permanent magnet synchronous machine drives at standstill considering inverter nonlinearities," *IEEE Trans. Power Electron.*, vol. 29, no. 12, pp. 6615–6627, Dec. 2014.

[5] K. Liu and Z. Q. Zhu, "Position-offset-based parameter estimation using the Adaline NN for condition monitoring of permanent-magnet synchronous machines," *IEEE Trans. Ind. Electron.*, vol. 62, no. 4, pp. 2372–2383, Apr. 2015.

[6] P. Wang, K. Lin, X. Zhang, S. Wang, J. Ai, and M. Lin, "An online estimation method for both stator inductance and rotor flux linkage of SPMSM without dead-time influence," *IEEE J. Emerg. Sel. Topics Power Electron.*, vol. 10, no. 2, pp. 1627–1638, Apr. 2022.

[7] K. Yu, Z. Wang, X. Wang, and Z. Zou, "An online flux estimation for dual three-phase SPMSM drives using position-offset injection," *IEEE Trans. Power Electron.*, vol. 36, no. 10, pp. 11606–11617, Oct. 2021.

[8] Q. Wang, G. Wang, N. Zhao, G. Zhang, Q. Cui, and D. Xu, "An impedance model-based multiparameter identification method of PMSM for both offline and online conditions," *IEEE Trans. Power Electron.*, vol. 36, no. 1, pp. 727–738, Jan. 2021.

[9] Y. Wang, Y. Xu, and J. Zou, "Online multiparameter identification method for sensorless control of SPMSM," *IEEE Trans. Power Electron.*, vol. 35, no. 10, pp. 10601–10613, Oct. 2020.

[10] Z. Li, G. Feng, C. Lai, D. Banerjee, W. Li, and N. C. Kar, "Current injection-based multi-parameter estimation for dual three-phase IPMSM considering VSI nonlinearity," *IEEE Trans. Transp. Electrific.*, vol. 5, no. 2, pp. 405–415, Jun. 2019.

[11] G. Feng, C. Lai, K. Mukherjee, and N. C. Kar, "Current injection-based online parameter and VSI nonlinearity estimation for PMSM drives using Current and voltage DC components," *IEEE Trans. Transp. Electrific.*, vol. 2, no. 2, pp. 119–128, Jun. 2016.

[12] Z. -H. Liu, H. -L. Wei, Q. -C. Zhong, K. Liu, X. -S. Xiao, and L. -H. Wu, "Parameter estimation for VSI-fed PMSM based on a dynamic PSO with learning strategies," *IEEE Trans. Power Electron.*, vol. 32, no. 4, pp. 3154–3165, Apr. 2017.

[13] W. Deng, C. Xia, Y. Yan, Q. Geng, and T. Shi, "Online multiparameter identification of surface-mounted PMSM considering inverter disturbance voltage," *IEEE Trans. Energy Convers.*, vol. 32, no. 1, pp. 202–212, Mar. 2017.

[14] Y. Yao, Y. Huang, F. Peng, J. Dong, and Z. Zhu, "Compensation method of position estimation error for high-speed surface-mounted PMSM drives based on robust inductance estimation," *IEEE Trans. Power Electron.*, vol. 37, no. 2, pp. 2033–2044, Feb. 2022.

[15] G. Xie, K. Lu, S. K. Dwivedi, R. J. Riber, and W. Wu, "Permanent magnet flux online estimation based on zero-voltage vector injection method," *IEEE Trans. Power Electron.*, vol. 30, no. 12, pp. 6506–6509, Dec. 2015.

[16] M. S. Rafaq, F. Mwasilu, J. Kim, H. H. Choi, and J. Jung, "Online parameter identification for model-based sensorless control of interior permanent magnet synchronous machine," *IEEE Trans. Power Electron.*, vol. 32, no. 6, pp. 4631–4643, Jun. 2017.

[17] D. Q. Dang, M. S. Rafaq, H. H. Choi, and J. W. Jung, "Online parameter estimation technique for adaptive control applications of interior PM synchronous motor drives," *IEEE Trans. Ind. Electron.*, vol. 63, no. 3, pp. 1438–1449, Mar. 2016.

[18] S. J. Underwood and I. Husain, "Online parameter estimation and adaptive control of permanent-magnet synchronous machines," *IEEE Trans. Ind. Electron.*, vol. 57, no. 7, pp. 2435–2443, Jul. 2010.

[19] Y. Shi, K. Sun, L. Huang, and Y. Li, "Online identification of permanent magnet flux based on extended kalman filter for IPMSM drive with position sensorless control," *IEEE Trans. Ind. Electron.*, vol. 59, no. 11, pp. 4169–4178, Nov. 2012.

[20] Z. H. Liu, H. L. Wei, X. H. Li, K. Liu, and Q. C. Zhong, "Global identification of electrical and mechanical parameters in PMSM drive based on dynamic self-learning PSO," *IEEE Trans. Power Electron.*, vol. 33, no. 12, pp. 10858–10871, Dec. 2018.

[21] X. Li and R. Kennel, "General formulation of Kalman-filter-based online parameter identification methods for VSI-Fed PMSM," *IEEE Trans. Ind. Electron.*, vol. 68, no. 4, pp. 2856–2864, Apr. 2021.

[22] K. Liu and Z. Q. Zhu, "Online estimation of the rotor flux linkage and voltage-source inverter nonlinearity in permanent magnet synchronous machine drives," *IEEE Trans. Power Electron.*, vol. 29, no. 1, pp. 418–427, Jan. 2014.

[23] M. X. Bui, M. F. Rahman, D. Guan, and D. Xiao, "A new and fast method for on-line estimation of d and q axes inductances of interior permanent magnet synchronous machines using measurements of current derivatives and inverter DC-bus voltage," *IEEE Trans. Ind. Electron.*, vol. 66, no. 10, pp. 7488–7497, Oct. 2019.

[24] R. Raja, T. Sebastian, and M. Wang, "Online stator inductance estimation for permanent magnet motors using PWM excitation," *IEEE Trans. Transp. Electrific.*, vol. 5, no. 1, pp. 107–117, Mar. 2019.

[25] S. Xiao and A. Griffo, "PWM-based flux linkage and rotor temperature estimations for permanent magnet synchronous machines," *IEEE Trans. Power Electron.*, vol. 35, no. 6, pp. 6061–6069, Jun. 2020.

[26] Q. Wang, G. Zhang, G. Wang, C. Li, and D. Xu, "Offline parameter self-learning method for general-purpose PMSM drives with estimation error compensation," *IEEE Trans. Power Electron.*, vol. 34, no. 11, pp. 11103–11115, Nov. 2019.

[27] D. Mingardi, M. Morandin, S. Bolognani, and N. Bianchi, "On the proprieties of the differential cross-saturation inductance in synchronous machines," *IEEE Trans. Ind. Appl.*, vol. 53, no. 2, pp. 991–1000, Mar./Apr. 2017.

[28] A. Balamurali, A. K. Anik, W. Clandfield, and N. C. Kar, "Non-invasive parameter and loss determination in PMSM considering the effects of saturation, cross-saturation, time harmonics, and temperature variations," *IEEE Trans. Magn.*, vol. 57, no. 2, pp. 1–6, Feb. 2021.

[29] K. Lee, J. I. Ha, and D. V. Simili, "Analysis and suppression of slotting and cross-coupling effects on current control in PM synchronous motor drives," *IEEE Trans. Power Electron.*, vol. 34, no. 10, pp. 9942–9956, Oct. 2019.

[30] B. Stumberger, G. Stumberger, D. Dolinar, A. Hamler, and M. Trlep, "Evaluation of saturation and cross-magnetization effects in interior permanent-magnet synchronous motor," *IEEE Trans. Ind. Appl.*, vol. 39, no. 5, pp. 1264–1271, Sep./Oct. 2003.
[31] Y. Yu et alet al., "Full parameter estimation for permanent magnet synchronous motors," *IEEE Trans. Ind. Electron.*, vol. 69, no. 5, pp. 4376–4386, May 2022.
[32] C. Wu, Y. Zhao, and M. Sun, "Enhancing low-speed sensorless control of PMSM using phase voltage measurements and online multiple parameter identification," *IEEE Trans. Power Electron.*, vol. 35, no. 10, pp. 10700–10710, Oct. 2020.
[33] G. Feng, C. Lai, X. Tan, W. Peng, and N. C. Kar, "Multi-parameter estimation of PMSM using differential model with core loss compensation," *IEEE Trans. Transp. Electrific.*, vol. 8, no. 1, pp. 1105–1115, Mar. 2022.
[34] A. Varatharajan, G. Pellegrino, G. B. Mariani, N. Voyer, and A. Satake, "LUT-less sensorless control of synchronous reluctance machines using the locus of incremental saliency ratio tracking (LIST)," *IEEE Trans. Ind. Electron.*, vol. 69, no. 7, pp. 6530–6539, Jul. 2022.
[35] D. F. Laborda, D. Díaz Reigosa, D. Fernández, K. Sasaki, T. Kato, and F. Briz, "Enhanced torque estimation in variable leakage flux PMSM combining high and low frequency signal injection," in *Proc. IEEE Energy Convers. Congr. Expo.*, 2020, pp. 1764–1771.
[36] J. Bonifacio and R. M. Kennel, "On considering saturation and cross-coupling effects for copper loss minimization on highly anisotropic synchronous machines," *IEEE Trans. Ind. Appl.*, vol. 54, no. 5, pp. 4177–4185, Sep./Oct. 2018.
[37] J. Bonifacio and R. Kennel, "Energy efficient control of synchronous machines in deep field-weakening operation including saturation effects," in *Proc. IEEE 15th Braz. Power Electron. Conf. 5th IEEE Southern Power Electron. Conf.*, 2019, pp. 1–6.

Shaobo Liu received the B.S. and M.S. degrees in electrical engineering in 2018 and 2020, respectively, from the Harbin Institute of Technology, Harbin, China, where he is currently working toward the Ph.D. degree in power electronics and electrical drives.

His current research interests include high efficiency ac–dc converter, PMSM parameter identification technique, and application of GaN power devices.

Qiwei Wang received the B.S., M.S., and Ph.D. degrees in electrical engineering from the Harbin Institute of Technology, Harbin, China, in 2015, 2017, and 2022, respectively.

He is currently an Assistant Professor with the School of Electrical Engineering and Automation, Harbin Institute of Technology. His current research interests include parameter identification technique, and PMSM position sensorless control.

Gaolin Wang (Senior Member, IEEE) received the B.S., M.S., and Ph.D. degrees in electrical engineering from the Harbin Institute of Technology, Harbin, China, in 2002, 2004, and 2008, respectively.

In 2009, he was with the Department of Electrical Engineering, Harbin Institute of Technology as a Lecturer, where he has been a Full Professor of Electrical Engineering since 2014. From 2009 to 2012, he was a Postdoctoral Fellow with Shanghai Step Electric Corporation. He has authored more than 70 technical papers published in IEEE Transactions. He is the holder of 40 Chinese patents. His current major research interests include permanent magnet synchronous motor drives and power converters.

Dr. Wang was a Guest Associate Editor for IEEE TRANSACTIONS ON INDUSTRIAL ELECTRONICS, an Associate Editor for IEEE TRANSACTIONS ON TRANSPORTATION ELECTRIFICATION, and *IET Electric Power Applications*.

Binxing Li received the B.S. and Ph.D. degrees in electrical engineering from the Harbin Institute of Technology, Harbin, China, in 2017 and 2022, respectively.

His current research interests include permanent magnet synchronous motor drives, high efficiency ac–dc converter, and application of GaN power devices.

Dawei Ding (Member, IEEE) received the B.S. and M.S. degrees from Hefei University of Technology, Hefei, China, in 2014 and 2017, respectively, and the Ph.D. degree from Harbin Institute of Technology (HIT), Harbin, China, in 2021, all in electrical engineering.

He is currently an Assistant Professor with the School of Electrical Engineering and Automation, HIT. His current research interests include advanced control of permanent magnet synchronous motor drives and electrolytic capacitorless ac motor drives.

Guoqiang Zhang (Member, IEEE) received the B.S. degree from Harbin Engineering University, Harbin, China, in 2011, and the M.S. and Ph.D. degrees from the Harbin Institute of Technology, Harbin, China, in 2013 and 2017, respectively, all in electrical engineering.

He is currently a Postdoctoral Fellow and a Lecturer with the Department of Electrical Engineering, Harbin Institute of Technology. His current research interests include parameter identification technique, and control of electrical drives, with main focus on sensorless field-oriented control of interior permanent magnet synchronous machines.

Dr. Zhang serves as an Associate Editor for *Journal of Power Electronics*.

Dianguo Xu (Fellow, IEEE) received the B.S. degree in control engineering from Harbin Engineering University, Harbin, China, in 1982, and the M.S. and Ph.D. degrees in electrical engineering from the Harbin Institute of Technology (HIT), Harbin, China, in 1984 and 1989, respectively.

In 1984, he was an Assistant Professor with the Department of Electrical Engineering, HIT. Since 1994, he has been a Professor with the Department of Electrical Engineering, HIT. He was the Dean with the School of Electrical Engineering and Automation, HIT, from 2000 to 2010. He was the Vice President of HIT, from 2014 to 2020. He has authored or coauthored more than 600 technical papers. His research interests include motor drives, PMSM servo drives, renewable energy generation technology, and power quality mitigation.

Prof. Xu is the co-EIC for IEEE TRANSACTIONS ON POWER ELECTRONICS, and an Associate Editor for IEEE TRANSACTIONS ON INDUSTRIAL ELECTRONICS and IEEE JOURNAL OF EMERGING AND SELECTED TOPICS IN POWER ELECTRONICS. He is currently the Chairman of IEEE Harbin Section.